


## Influence of the rotational sense of two colliding laser beams on the radiation of an ultrarelativistic electron

L. Aliani and Q. Z. Lv \*

*Max-Planck-Institut für Kernphysik, Saupfercheckweg 1, 69117 Heidelberg, Germany*



(Received 26 July 2023; accepted 15 September 2023; published 6 October 2023)

With analytical treatment, the classical dynamics of an ultrarelativistic electron in two counterpropagating circularly polarized strong laser beams with either a corotating or counterrotating direction are considered. Assuming that the particle energy is the dominant scale in the setup, an approximate solution is derived, and the influence of the rotational sense on the dynamics is analyzed. Qualitative differences in both electron energy and momentum are found between the corotating and counterrotating laser beams and are confirmed by the exact numerical solution of the classical equation of motion. Despite these differences in the electron trajectory, the radiation spectra of the electron do not deviate qualitatively from each other for configurations with a varying rotational sense of the laser beams. Here, the radiation of an ultrarelativistic electron interacting with counterpropagating laser beams is given in the framework of the Baier-Katkov semiclassical approximation. Several parameter regimes are considered, and the spectra resulting from the two scenarios all have the same shape and only differ quantitatively by a few percent.

DOI: [10.1103/PhysRevA.108.042204](https://doi.org/10.1103/PhysRevA.108.042204)

### I. INTRODUCTION

Ultrastrong-laser techniques, both those presently available [1,2] and near-future facilities [3,4], will allow investigation into extreme regimes of nonlinear quantum electrodynamics (QED) processes.  $\gamma$  photons can be produced by electron radiation, which may further generate avalanches of electron-positron pairs through cascade processes [5–11]. Multiple-photon emissions and large quantum recoils of emitted photons result in the emergence of conspicuous classical and quantum radiation reaction effects [12,13]. In the realm of standard QED, these nonlinear processes correspond to the inclusion of higher orders of perturbation expansions, which yield numerous Feynman diagrams and render the calculation intractable. In order to overcome this obstacle, strong-field QED has been introduced [14], which replaces the free-particle wave function in the calculations with the wave function in the presence of the strong field under consideration. Since the strong field is regarded as a classical field here, the transition from standard to strong-field QED is determined by the dimensionless field strength  $\xi \equiv -eE_0/m\omega_0$ , where  $e$  and  $m$  are the electron charge and mass, respectively,  $E_0$  is the electric-field amplitude, and  $\omega_0$  is the angular frequency of the strong field. (Relativistic units  $\hbar = c = 1$  are used throughout the paper, unless specified otherwise.)

Unfortunately, the exact analytical wave functions for an electron in strong classical fields exist for only a few special field configurations [15]. For a general configuration, several approximate approaches are developed to investigate the nonlinear QED processes. For very high field intensities ( $\xi \gg 1$ ), the most common method is to approximate the strong electromagnetic field as a locally constant crossed electric and magnetic field. However, deficiencies and breakdowns of the local constant-field approximation (LCFA) were observed in various regimes recently [16–23]. An alternative approach is the so-called Wentzel-Kramers-Brillouin (WKB) approximation [24–30]. It is closely connected to the classical description and can be obtained only in cases in which the electron's classical equation of motion is solvable. Inspired by the spirit of the WKB approximation, Baier and Katkov developed the semiclassical operator approach, which can express the amplitudes of strong-field QED processes (e.g., nonlinear Compton and nonlinear Breit-Wheeler) in complex general background fields as a function of the electron's classical trajectory [31–33] when there is no exact solution for the corresponding Dirac equation.

The experimental limit of investigating the strong-field QED processes is the field strength obtained in the laboratory. The desire to increase the effective field strength even more with a fixed laser-beam energy gave rise to the concept of multibeam configurations [34,35] and the notion of a dipole wave [36–39]. One of the simplest cases of a multibeam configuration is the counterpropagating-wave (CPW) setup, which is an attractive setup to study strong-field QED effects [40–44] and a favorable configuration for QED cascades [45,46] and new x-ray sources [47]. Especially, the field configuration of a rotating electric field, which mimics the antinode of a standing wave, is widely used to study the pair-creation mechanism [48–51]. It is also noteworthy that

\*qingzheng.lyu@mpi-hd.mpg.de

*Published by the American Physical Society under the terms of the Creative Commons Attribution 4.0 International license. Further distribution of this work must maintain attribution to the author(s) and the published article's title, journal citation, and DOI. Open access publication funded by the Max Planck Society.*

in this setup electron-trapping dynamics are also observable, which strongly depend on the particle dynamics due to the radiation reaction [42,52]. The dynamics of a particle in the presence of the CPW configuration are determined by the ratio of the laser frequencies as seen in the electron's average rest frame. If this ratio is close to unity, the system is resonant, giving rise to phenomena such as the Kapitza-Dirac effect [53–56] and stimulated Compton emission [57–60]. The latter is the operating principle for free-electron lasers [61]. On the other hand, the classical and quantum equations of motion for an electron have also been investigated in the nonresonant regime, where the above-mentioned ratio is far from 1, by using various approaches [62–64].

In this work, the classical dynamics and the radiation processes of an ultrarelativistic electron moving in a circularly polarized CPW are considered in the nonresonant regime for both co- and counterrotating arrangements of the two laser beams. The classical trajectory of the electron is obtained both analytically and numerically. We generalized the approach employed in Ref. [64], where the analytical solution is based on an approximation that imposed a restriction on the laser parameters and the electron's initial momentum; namely, the electron's average energy must be the dominant energy scale in the system ( $\xi_1 \xi_2 \ll \gamma^2$ , with  $\xi_1$  and  $\xi_2$  being the laser fields' strengths and  $\gamma$  being the average Lorentz factor of the electron in the fields). This solution is verified by a fully numerical calculation. By substituting this analytical solution into the Baier-Katkov (BK) operator method, we also studied the radiation properties of the electron in the background field. Particularly, the change in the radiation spectrum caused by modifying the lasers' rotational sense is investigated. The investigation shows that although the dynamics are qualitatively different in the co- or counterrotating cases, the radiation spectra of the electron have a similar shape and differ only quantitatively by a few percent.

This paper is organized as follows. Section II gives the derivations of the electron's classical trajectory in the CPW with arbitrary rotational sense and compares it with a fully numerical solution. The influence of the laser's direction of rotation on the electron dynamics is investigated. The calculation of the photon-emission matrix elements and the corresponding emission formula are given in Sec. III. By employing the emission-probability formula, we also analyze the effects of the sense of rotation on the radiation spectrum. Finally, we conclude our paper in Sec. IV with a discussion of our main findings.

## II. THE CLASSICAL DYNAMICS

In this section the mathematical formulation of the CPW problem is introduced. The approximated solution and its validity condition are derived for arbitrary rotational sense of the lasers. The classical equation of motion for an electron in the presence of an electromagnetic field reads

$$\frac{dP^\mu}{d\tau} = \frac{e}{m} F^{\mu\nu} P_\nu, \quad (1)$$

where  $\tau$  is the proper time,  $P_\mu$  is the particle's four-momentum, and  $F_{\mu\nu} \equiv \partial_\mu A_\nu - \partial_\nu A_\mu$  is the electromagnetic field tensor. The vector potential corresponding to the CPW

configuration is  $A = A_1 + A_2$ , where

$$\begin{aligned} A_1 &\equiv a_1 g_1(\phi_1) [\cos \phi_1 e_x + \epsilon_1 \sin \phi_1 e_y], \\ A_2 &\equiv a_2 g_2(\phi_2) [\cos \phi_2 e_x + \epsilon_2 \sin \phi_2 e_y], \end{aligned} \quad (2)$$

with the scalars  $a_1$  and  $a_2$  being the field amplitudes, the function  $g_{1,2}(\phi)$  denoting the slow wave envelopes, and  $\epsilon_{1,2}$  being +1 or -1, corresponding to a leftwards or rightwards rotation of the wave, respectively. In the following we use the normalized value  $\xi_{1,2} = -ea_{1,2}/m$  for the field strength, while  $e_x = (0, 1, 0, 0)$  and  $e_y = (0, 0, 1, 0)$  are unit vectors. We choose the optical frequency  $\omega = 1.55$  eV for the lasers in this work. Furthermore, the classical trajectory is related to the momentum according to

$$\mathbf{x}(\tau) = \int d\tau \frac{\mathbf{P}(\tau)}{m}. \quad (3)$$

An exact solution for Eq. (1) in the background field of the CPW is not feasible, and some approximations need to be applied to obtain the classical trajectory. The main task of solving Eq. (1) is to integrate over the proper time  $\tau$ . Therefore, to help us perform the integral in Eq. (3), we claim that we can rewrite phases  $\phi_1$  and  $\phi_2$  in Eq. (2) as

$$\begin{aligned} \phi_1 &= k_1 \cdot x(\tau) = \frac{k_1 \cdot \bar{P}}{m} \tau + \delta\phi_1(\tau), \\ \phi_2 &= k_2 \cdot x(\tau) = \frac{k_2 \cdot \bar{P}}{m} \tau + \delta\phi_2(\tau), \end{aligned} \quad (4)$$

with

$$\delta\phi_1 = \int \frac{k_1 \cdot \delta P(\tau)}{m} d\tau, \quad \delta\phi_2 = \int \frac{k_2 \cdot \delta P(\tau)}{m} d\tau \quad (5)$$

being the higher-order corrections. Here, the wave vectors read  $k_1 = (\omega, 0, 0, \omega)$ ,  $k_2 = (\omega, 0, 0, -\omega)$ , and  $\delta P(\tau) = P(\tau) - \bar{P}$ , with the bar symbol indicating the averaged quantity, which can be obtained by averaging the time-dependent quantities over the proper time  $\tau$  inside the laser fields. If the envelope functions  $g_1(\phi_1)$  and  $g_2(\phi_2)$  are smooth enough, which implies the two lasers are turned on adiabatically, we can write down the analytical expression relating the asymptotic momentum to the average momentum in the laser fields [64]. In the case of the  $\xi_1$  laser being turned on first, this relation is

$$\bar{P}^\mu = p^\mu + \frac{m^2 \xi_1^2}{2(k_1 \cdot p)} k_1^\mu + \frac{m^2 \xi_2^2}{2[k_2 \cdot \bar{P}^{(1)}]} k_2^\mu, \quad (6)$$

where

$$\bar{P}_\mu^{(1)} = p_\mu + \frac{m^2 \xi_1^2}{2(k_1 \cdot p)} k_{1,\mu}. \quad (7)$$

If the  $\xi_2$  laser is turned on first, it analogously reads

$$\bar{P}^\mu = p^\mu + \frac{m^2 \xi_1^2}{2[k_1 \cdot \bar{P}^{(2)}]} k_1^\mu + \frac{m^2 \xi_2^2}{2(k_2 \cdot p)} k_2^\mu, \quad (8)$$

with

$$\bar{P}_\mu^{(2)} = p_\mu + \frac{m^2 \xi_2^2}{2(k_2 \cdot p)} k_{2,\mu}. \quad (9)$$

When both lasers are turned on simultaneously, the electron behaves as if the counterpropagating laser beams had been turned on first since the copropagating beam oscillates much more slowly in the electron's rest frame.

### A. Analytical solutions

Now, let us try to integrate over Eq. (1). To do this, we assume that the higher-order corrections in Eq. (4) can be ignored and the following integrals can be performed:

$$\begin{aligned} \int d\tau \sin(\phi_1) &\approx -\frac{m}{k_1 \cdot \bar{P}} \cos(\phi_1), \\ \int d\tau \sin(\phi_2) &\approx -\frac{m}{k_2 \cdot \bar{P}} \cos(\phi_2), \\ \int d\tau \sin(\phi_1 - \phi_2) &\approx -\frac{m}{(k_1 - k_2) \cdot \bar{P}} \cos(\phi_1 - \phi_2), \\ \int d\tau \sin(\phi_1 + \phi_2) &\approx -\frac{m}{(k_1 + k_2) \cdot \bar{P}} \cos(\phi_1 + \phi_2), \end{aligned} \quad (10)$$

as well as the similar integral of  $\cos \rightarrow \sin$ . The condition under which this assumption is valid will be analyzed later. In the derivation below we set the envelopes  $g_{1,2}(\phi) = 1$  for reasons of simplicity because the lasers are assumed to be turned on adiabatically. However, these envelopes are important when we compare the analytical results with the numerical ones. We will discuss this in the next section.

Since the vector potential in Eq. (2) is independent of the transverse coordinates  $x$  and  $y$ , the canonical momenta in these directions are conserved, leading to

$$P_{\perp}(\tau) = p_{\perp} - eA(\tau). \quad (11)$$

Without loss of generality, we choose the initial transverse momentum  $p_{\perp}$  to be only along the  $x$  axis. Substituting the explicit vector potential, one arrives at

$$P_x(\tau) = p_x + m\xi_1 \cos \phi_1 + m\xi_2 \cos \phi_2, \quad (12)$$

$$P_y(\tau) = m\xi_1 \epsilon_1 \sin \phi_1 + m\xi_2 \epsilon_2 \sin \phi_2. \quad (13)$$

With the substitution of these transverse momenta and the magnetic-field components of the laser field

$$\mathbf{B}_1 = -\omega a_1 (-\epsilon_1 \cos \phi_1 \hat{\mathbf{x}} - \sin \phi_1 \hat{\mathbf{y}}), \quad (14)$$

$$\mathbf{B}_2 = \omega a_2 (-\epsilon_2 \cos \phi_2 \hat{\mathbf{x}} - \sin \phi_2 \hat{\mathbf{y}}), \quad (15)$$

the equation obeyed by the momentum along the  $z$  direction is

$$\begin{aligned} \frac{dP_z}{d\tau} &= -p_x \omega [\xi_1 \sin \phi_1 - \xi_2 \sin \phi_2] \\ &\quad - m\xi_1 \xi_2 \omega (1 + \epsilon_1 \epsilon_2) \sin(\phi_1 - \phi_2). \end{aligned} \quad (16)$$

After integrating over  $\tau$ , we arrive at

$$\begin{aligned} P_z &= \bar{P}_z + p_x \omega \left[ \frac{m\xi_1}{k_1 \cdot \bar{P}} \cos \phi_1 - \frac{m\xi_2}{k_2 \cdot \bar{P}} \cos \phi_2 \right] \\ &\quad + \frac{m^2 \omega \xi_1 \xi_2 \epsilon_-}{(k_1 - k_2) \cdot \bar{P}} \cos(\phi_1 - \phi_2), \end{aligned} \quad (17)$$

with  $\epsilon_- = 1 + \epsilon_1 \epsilon_2$ . After the expressions for all momenta have been derived, the energy of the electron in the laser fields can be obtained based on the energy-momentum relation

$$\varepsilon = (m^2 + P_x^2 + P_y^2 + P_z^2)^{1/2}. \quad (18)$$

By defining the time-averaged energy as  $\bar{\varepsilon} = \sqrt{m_*^2 + p_x^2 + \bar{P}_z^2}$ , with  $m_* = m\sqrt{1 + \xi_1^2 + \xi_2^2}$  being the effective mass of the

electron in the laser fields, the energy can be rewritten as

$$\varepsilon = \bar{\varepsilon} + \delta\varepsilon + \bar{\varepsilon} O\left(\frac{\delta P_z}{\bar{\varepsilon}}\right)^2 + \bar{\varepsilon} O\left(\frac{\delta\varepsilon}{\bar{\varepsilon}}\right)^2, \quad (19)$$

where we applied the Taylor expansion. The oscillating term in the energy looks like

$$\begin{aligned} \delta\varepsilon &= p_x \omega \left( \frac{m\xi_1}{k_1 \cdot \bar{P}} \cos \phi_1 + \frac{m\xi_2}{k_2 \cdot \bar{P}} \cos \phi_2 \right) \\ &\quad + \frac{m^2 \omega \xi_1 \xi_2 \epsilon_+}{(k_1 + k_2) \cdot \bar{P}} \cos(\phi_1 + \phi_2), \end{aligned} \quad (20)$$

with  $\epsilon_+ = 1 - \epsilon_1 \epsilon_2$ . In order for the expansion in Eq. (19) to be valid, we need  $O(\frac{\delta P_z}{\bar{\varepsilon}}) \ll 1$  and  $O(\frac{\delta\varepsilon}{\bar{\varepsilon}}) \ll 1$ , which yields the following conditions:

$$\begin{aligned} \frac{m\xi_1 p_x \omega}{k_1 \cdot \bar{P} \bar{\varepsilon}} &\ll 1, \quad \frac{m^2 \xi_1 \xi_2 \omega}{(k_1 + k_2) \cdot \bar{P} \bar{\varepsilon}} \ll 1, \\ \frac{m\xi_2 p_x \omega}{k_2 \cdot \bar{P} \bar{\varepsilon}} &\ll 1, \quad \frac{m^2 \xi_1 \xi_2 \omega}{(k_1 - k_2) \cdot \bar{P} \bar{\varepsilon}} \ll 1. \end{aligned} \quad (21)$$

So far, we have not given the explicit form of phases  $\phi_1$  and  $\phi_2$ . But substituting energy and momentum into Eq. (5) allows us to write the higher-order terms of the phases as

$$\begin{aligned} \delta\phi_1 &= \Phi_1 + C_1 \sin(\phi_2) - C_{1-2} \sin(\phi_1 - \phi_2) \\ &\quad + C_{1+2} \sin(\phi_1 + \phi_2), \end{aligned} \quad (22)$$

$$\begin{aligned} \delta\phi_2 &= \Phi_2 + C_2 \sin(\phi_1) + C_{1-2} \sin(\phi_1 - \phi_2) \\ &\quad + C_{1+2} \sin(\phi_1 + \phi_2), \end{aligned} \quad (23)$$

where the coefficients are

$$\begin{aligned} C_1 &= \frac{2p_x m \xi_2 \omega^2}{(k_2 \cdot \bar{P})^2}, \quad C_{1-2} = \frac{\epsilon_- m^2 \xi_1 \xi_2 \omega^2}{[(k_1 - k_2) \cdot \bar{P}]^2}, \\ C_2 &= \frac{2p_x m \xi_1 \omega^2}{(k_1 \cdot \bar{P})^2}, \quad C_{1+2} = \frac{\epsilon_+ m^2 \xi_1 \xi_2 \omega^2}{[(k_1 + k_2) \cdot \bar{P}]^2}. \end{aligned} \quad (24)$$

Now, with Eqs. (4), (22), and (23), we have an implicit system for the solution of the phases. Without loss of generality, we now choose the electron to copropagate along  $\xi_1$ , which results in only  $C_2$  being non-negligible. In order to make sure that the contributions of  $C_1$ ,  $C_{1+2}$ , and  $C_{1-2}$  to the momentum are second order and the key assumption in Eq. (10) indeed holds, we follow a procedure similar to the one shown in Ref. [64] and obtain further restrictions for our solution. These can be written as

$$\begin{aligned} \frac{2p_x m \xi_1 \omega^2}{(k_1 \cdot \bar{P})(k_2 \cdot \bar{P})} &\ll 1, \\ \frac{2p_x m \xi_1 \omega^2}{(k_1 \cdot \bar{P})[(k_1 - k_2) \cdot \bar{P}]} &\ll 1, \\ \frac{2p_x m \xi_1 \omega^2}{(k_1 \cdot \bar{P})[(k_1 + k_2) \cdot \bar{P}]} &\ll 1. \end{aligned} \quad (25)$$

Thus, combining the conditions in Eqs. (21) and (25) yields the concluding validity criteria for the solution,

$$\frac{m^2 \xi_2 \xi_1}{2\bar{\varepsilon}^2} \ll 1, \quad \frac{2p_x m \xi_1}{m_*^2} \ll 1, \quad \frac{p_x m \xi_2}{2\bar{\varepsilon}^2} \ll 1. \quad (26)$$

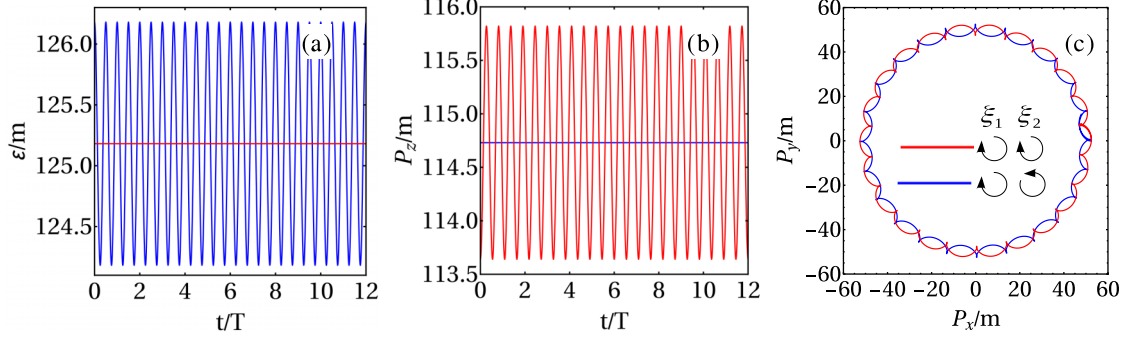


FIG. 1. The four-momentum of the electron in the CPW laser fields with  $\xi_1 = 50$  and  $\xi_2 = 2.5$ . The average energy is chosen to be  $\bar{\epsilon} = 125m$ , and the initial transverse momentum  $p_x = 0$ . The electron is, on average, propagating along with  $\xi_1$ . In (a) and (b), the energy  $\epsilon$  and momentum  $P_z$  are shown as a function of the interaction time. In (c), the motion of the electron in the  $P_x$ - $P_y$  plane is portrayed. The blue curves denote the counterrotating case ( $\epsilon_1\epsilon_2 = -1$ ), while the red curves denote the corotating case ( $\epsilon_1\epsilon_2 = 1$ ).  $T = 2\pi/\omega$  is the laser period in the laboratory frame.

For the case of the electron copropagating with the  $\xi_2$  laser, the conditions will be the similar with  $\xi_1 \leftrightarrow \xi_2$ .

Finally, the classical four-momentum can be written in a covariant form as

$$\begin{aligned} P^\mu = \bar{P}^\mu - e[A_1^\mu(\phi_1) + A_2^\mu(\phi_2)] + k_1^\mu \left[ \frac{e p \cdot A_1(\phi_1)}{k_1 \cdot \bar{P}} + \frac{\epsilon_+ e^2 A_1^\mu(\phi_1) \cdot A_2^\mu(\phi_2)}{2(k_1 + k_2) \cdot \bar{P}} - \frac{\epsilon_- e^2 A_1^\mu(\phi_1) \cdot A_2^\mu(\phi_2)}{2(k_1 - k_2) \cdot \bar{P}} \right] \\ + k_2^\mu \left[ \frac{e p \cdot A_2(\phi_2)}{k_2 \cdot \bar{P}} + \frac{\epsilon_+ e^2 A_1^\mu(\phi_1) \cdot A_2^\mu(\phi_2)}{2(k_1 + k_2) \cdot \bar{P}} + \frac{\epsilon_- e^2 A_1^\mu(\phi_1) \cdot A_2^\mu(\phi_2)}{2(k_1 - k_2) \cdot \bar{P}} \right], \end{aligned} \quad (27)$$

with  $p_\mu$  being the asymptotic momentum and  $\epsilon_- = 2, \epsilon_+ = 0$  for the corotating case and  $\epsilon_- = 0, \epsilon_+ = 2$  for the counterrotating case. One can verify that in the corotating case, the formula recovers the results in Ref. [64]. Additionally, in the case that one of the laser beams vanishes, our result recovers the familiar plane-wave solution [65]. With the momentum being determined now, we can write down the trajectory of the electron as a function of the proper time based on Eq. (3) as

$$\begin{aligned} t = \frac{\bar{\epsilon}}{m} \tau + p_x \omega \left( \frac{m \xi_1}{(k_1 \cdot \bar{P})^2} \sin \phi_1 + \frac{m \xi_2}{(k_2 \cdot \bar{P})^2} \sin \phi_2 \right) + \frac{m^2 \omega \xi_1 \xi_2 \epsilon_+}{[(k_1 + k_2) \cdot \bar{P}]^2} \sin(\phi_1 + \phi_2), \\ x = \frac{p_x}{m} \tau + \frac{m \xi_1}{k_1 \cdot \bar{P}} \sin \phi_1 + \frac{m \xi_2}{k_2 \cdot \bar{P}} \sin \phi_2, \quad y = -\frac{m \xi_1 \epsilon_1}{k_1 \cdot \bar{P}} \cos \phi_1 - \frac{m \xi_2 \epsilon_2}{k_2 \cdot \bar{P}} \cos \phi_2, \\ z = \frac{\bar{P}_z}{m} \tau + p_x \omega \left( \frac{m \xi_1}{(k_1 \cdot \bar{P})^2} \sin \phi_1 - \frac{m \xi_2}{(k_2 \cdot \bar{P})^2} \sin \phi_2 \right) + \frac{m^2 \omega \xi_1 \xi_2 \epsilon_-}{[(k_1 - k_2) \cdot \bar{P}]^2} \sin(\phi_1 - \phi_2). \end{aligned} \quad (28)$$

## B. Numerical results

With the analytical expressions for the electron's momenta and coordinates being derived, we study in this section the main properties of the motion, with emphasis on the dissimilarities between the cases of co- and counterrotating laser fields. From Eq. (27), we can see that there are two main differences. The first difference is the sense of rotation in the  $x$ - $y$  plane as  $P_y$  changes its direction between the co- and counterrotating cases. The second one is the crossing term proportional to  $\xi_1 \xi_2$ . For the corotating case, the crossing term emerges in the momentum  $P_z$ , while in the counterrotating case it appears in the energy  $\epsilon$ .

We inspect the electron's four-momentum for both the co- and counterrotating cases in Fig. 1, where we compare different behaviors between the two cases. The results shown in Fig. 1 are based on Eq. (27) but are proved by the fully numerical solutions of Eq. (1). The average energy is  $\bar{\epsilon} = 125m$ ,

corresponding to  $\omega_2/\omega_1 = 22.95$ . Here,  $\omega_{1,2} \equiv k_{1,2} \cdot \bar{P}/\bar{\epsilon}$  are the laser frequencies in the electron's rest frame. The plots represent a time interval of one cycle of the  $\xi_1$  beam and 23 cycles of the  $\xi_2$  beam as the electron is propagating along with  $\xi_1$  on average.

By choosing a vanishing transverse momentum, we can see, from Fig. 1(a), that the energy is a constant for the corotating case but oscillates around the same constant for the counterrotating one. The amplitude of the oscillation is proportional to  $\xi_1 \xi_2 / \bar{\epsilon}$ , and the frequency of the oscillation is approximately  $\omega_2$  as  $\omega_2/\omega_1 \gg 1$ . On the other hand, the behavior of the momentum along the  $z$  direction in Fig. 1(b) is exactly swapped.  $P_z$  for the corotating case oscillates around the constant  $P_z$  of the counterrotating case with an amplitude proportional to  $\xi_1 \xi_2 / \bar{P}_z$ . The frequency is the same as the one for the oscillations in the energy [Fig. 1(a)] since from Eq. (27) we can see that the crossing terms are both dependent

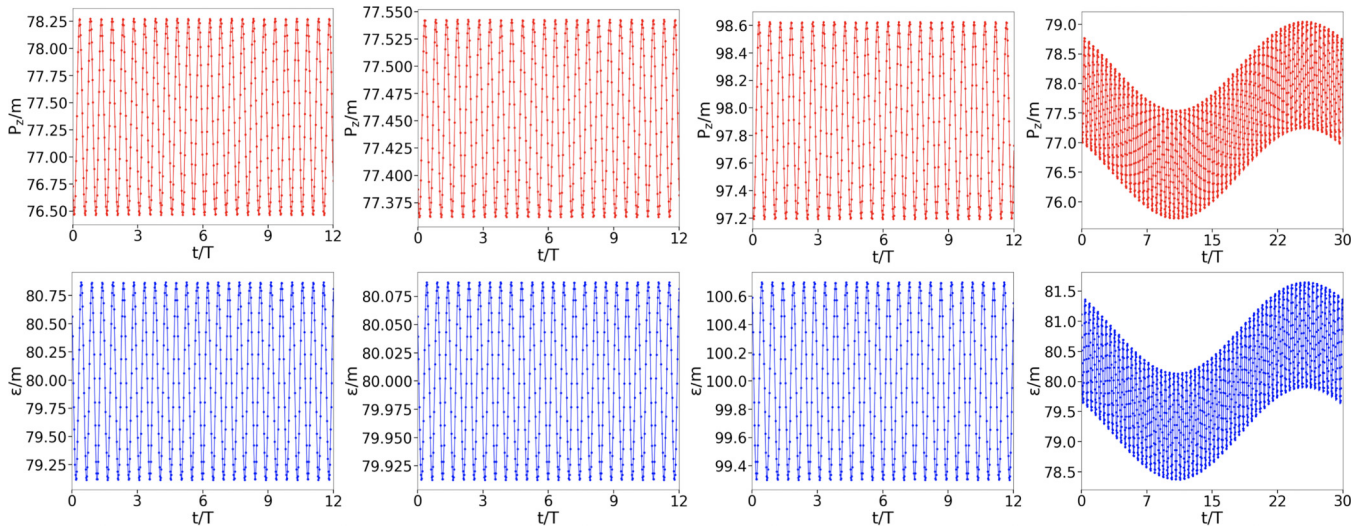


FIG. 2. The momentum  $P_z$  for the corotating case and the energy  $\varepsilon$  for the counterrotating case are displayed as a function of the interaction time. The top row shows the corotating case (red), while the bottom row shows the counterrotating case (blue). The solid lines are the analytical results based on Eq. (27), and the dots are the numerical solution of Eq. (1). In all the panels, we choose  $\xi_1 = 20$ . The strength of the second laser is chosen to be  $\xi_2 = 3.5$ , except in the second column, where  $\xi_2 = 0.35$ . The average energy is chosen to be  $\bar{\varepsilon} = 80m$  for the first, second, and fourth columns, while for the third column we choose  $\bar{\varepsilon} = 100m$ . The transverse momentum  $p_x$  is  $0.1m$  for the last column; otherwise, it is zero.

on  $\phi_1$  and  $\phi_2$ , with the much bigger  $\phi_2$  dominating over the smaller  $\phi_1$ .

In Fig. 1(c), the momentum in the transverse plane is displayed. Equation (27) shows us that oscillations in  $P_x$  and  $P_y$  consist of two parts. One of them is related to the  $\xi_1$  laser. Since the electron is propagating along with  $\xi_1$ , this oscillation gives the large enclosing circle, which is of size  $m\xi_1$ . The small-amplitude and high-frequency oscillations caused by the  $\xi_2$  laser then gave the small kinks and arcs along the big  $\xi_1$  circle. The number of these arcs is related to  $\omega_2/\omega_1$  because it depends on how many  $\xi_2$  oscillations the electron is cycling through during one  $\xi_1$  oscillation and therefore depends linearly on the energy of the electron. The radius of the arc, on the other hand, depends on  $m\xi_2$ .

To show the accuracy of our analytical solutions, we compared the analytical result with the numerical one in Fig. 2. It was shown in Eq. (27) as well as in Fig. 1 that the higher-order oscillation, namely, the crossing term, appears only in  $\varepsilon$  for the counterrotating case and in  $P_z$  for the corotating case. Therefore, we plot the energy  $\varepsilon$  for the counterrotating case and the  $P_z$  momentum for the corotating case in Fig. 2.

Comparing the first column with the second one, we can see that the oscillation amplitude decreases by about one order of magnitude, while the average  $P_z$  (corotating) or  $\varepsilon$  (counterrotating) remains the same. This is because  $\xi_2$  decreases by one order of magnitude and the crossing term is proportional to it [see Eq. (27)]. By increasing the energy  $\varepsilon$  from  $80m$  (first column) to  $100m$  (third column), the oscillation amplitude decreases again because the prefactor of the crossing term is proportional to  $1/\varepsilon$  in the counterrotating case and  $1/P_z$  in the corotating case. In the fourth column, a transverse momentum of  $p_x = 0.1m$  is introduced. We observe now two kinds of oscillations in both  $\varepsilon$  and  $P_z$ . This is because if  $p_x \neq 0$ , the oscillation related solely to  $\xi_1$  or  $\xi_2$  in  $\varepsilon$  and  $P_z$  appears in addition to the crossing term. The fast oscillation is now the

result of two individual oscillations, which relate to  $\xi_2$  and the crossing term of  $\xi_1\xi_2$ .

In order to quantitatively characterize the disagreement between the numerical and analytical results, we introduce the relative deviation of the analytical prediction (subscript  $a$ ) of a quantity  $X$  with respect to the numerically calculated value (subscript  $n$ ) as follows:

$$\Delta_X \equiv \frac{1}{2T} \int_{-T}^T dt \left| \frac{X_a - X_n}{X_n} \right|, \quad (29)$$

with  $X$  being either the longitudinal momentum  $P_z$  for the corotating case or the energy  $\varepsilon$  for the counterrotating case. The integration time is taken to infinity, i.e.,  $T \rightarrow \infty$ . It should be noted that the phases  $\phi_1$  and  $\phi_2$  contain arbitrary constants  $\Phi_1$  and  $\Phi_2$ . In order to compare the analytical and numerical quantities these constants should be specified. We write down  $\Phi_1$  and  $\Phi_2$  as  $\Phi_1 = k_1 \cdot x_0$  and  $\Phi_2 = k_2 \cdot x_0$ , where  $x_0$  is the temporal and spatial location of the particle at the moment when the turn-on process in the numerical simulation is finished. In this case we can have the same initial phase for both analytical and numerical solutions. The relative difference for the four cases shown in Fig. 2 is calculated together with the conditions (26) of the analytical solutions in Table I.

From Table I, we can see that the relative difference between the numerical solution and the analytical solution is quite small within the parameter regime we consider and increases if the criteria are not well fulfilled anymore, for example, when the transverse momentum is introduced. This critical dependence on the transverse momentum also demands that the collision angle between the electron and the laser pulse is small. From Eq. (26), we can estimate this collision angle as  $\tan \theta = P_x/P_z \ll (1 + \xi_1^2 + \xi_2^2)/(2\gamma\xi_1)$ .

TABLE I. The relative difference in the energy  $\Delta_\varepsilon$  for the counterrotating case and in the longitudinal momentum  $\Delta_{p_z}$  for the corotating case with the same parameters as in Fig. 2.

Case	Criteria [Eq. (26)]	$\Delta_{p_z}$	$\Delta_\varepsilon$
First column	[0.011,0.0,0.0]	$1.05 \times 10^{-4}$	$7.84 \times 10^{-5}$
Second column	[0.001,0.0,0.0]	$2.87 \times 10^{-6}$	$7.68 \times 10^{-7}$
Third column	[0.007,0.0,0.0]	$4.68 \times 10^{-5}$	$3.58 \times 10^{-5}$
Fourth column	[0.011,0.010,0.00003]	$2.10 \times 10^{-4}$	$1.50 \times 10^{-4}$

The analytical results and all the analysis above concern monochromatic plane waves because the laser pulses are assumed to be turned on adiabatically. However, the laser pulses always have finite length in realistic experiments, especially for high intensity. In order to apply the analytics to a realistic scenario, we compare the analytics with the numerics for finite pulse length. From Fig. 3, we can see that the analytical results agree well with the numerics even for short pulse length. Here, we choose the pulse length of the  $\xi_1$  laser  $L_1$  as a parameter. In our scenario, the ultrarelativistic electron copropagates with the  $\xi_1$  laser and counterpropagates with the  $\xi_2$  laser. Because of the Doppler effect, the length of the  $\xi_2$  laser pulse needs to be at least  $n$  ( $= \omega_2/\omega_1 = 4\gamma_*^2 \gg 1$ ) times longer than the period of the  $\xi_1$  laser, such that the electron goes through at least one cycle of  $\xi_1$  during the overlap of the two lasers. Otherwise, for a short  $\xi_2$  laser, the dynamic of the electron will be mainly controlled by the  $\xi_2$  laser because the  $\xi_1$  laser will act only as a constant field in this case. Therefore, the length of the  $\xi_1$  laser plays a dominant role in the application of the analytics in a realistic situation.

The small relative difference with respect to the exact numerical solution now gives us the justification to employ the analytical solution to study the radiation of an ultrarelativistic electron in a CPW setup within certain parameter regimes.

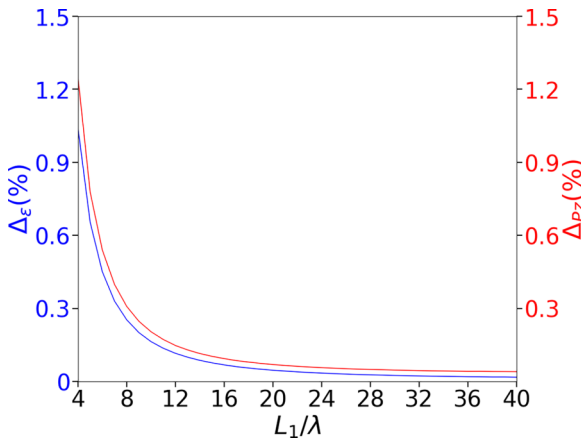


FIG. 3. The relative difference between the finite-pulse-length (numerical) results and the infinite-pulse-length (analytical) results regarding the energy  $\Delta_\varepsilon$  (blue line) for the counterrotating case and regarding the longitudinal momentum  $\Delta_{p_z}$  (red line) for the corotating case. Here, we choose the envelope functions  $g_{1,2}(\phi)$  to be  $\cos^2(\phi/L)$  during the switch-on and -off process. We compare the analytics and numerics in one cycle of the  $\xi_1$  laser after the switch-on. The other parameters are the same as in the first column in Fig. 2

### III. QUANTUM RADIATION

#### A. Radiation formulas

If the classical trajectory is applied, the emission can be calculated according to the Baier-Katkov method [31–33]. For the sake of simplicity, we start with a spinless particle. An analogous derivation for the spinor case is given later. The Baier-Katkov expression for the emitted intensity  $dI$  reads

$$dI = \frac{\alpha \varepsilon}{(2\pi)^2 \varepsilon' T_0} |\mathcal{T}_\mu|^2 d^3 k', \quad (30)$$

where  $\alpha$  is the fine-structure constant,  $T_0$  is the interaction time, and  $\varepsilon' = \varepsilon - \omega'$  is the energy of the electron after the emission of a photon. The transition amplitude

$$\mathcal{T}_\mu(k') = \int_{-\infty}^{\infty} dt v_\mu(t) e^{i\psi}, \quad \psi \equiv \frac{\varepsilon}{\varepsilon'} k' \cdot x(t), \quad (31)$$

with  $v_\mu = dx_\mu/dt$ .  $k'_\mu$  is the emitted photon four-momentum, characterized by its energy  $\omega'$  and the emission direction  $\mathbf{n} = (\cos \varphi \sin \theta, \sin \varphi \sin \theta, \cos \theta)$  as

$$k'_\mu = \omega'(1, \mathbf{n}). \quad (32)$$

Within the realm of this theory, the oscillation of  $\delta\varepsilon$  is assumed to be small compared to  $\varepsilon$ , which holds in our case, as shown in the previous section. Accordingly, the factor appearing in the phase may be approximated as  $\frac{\varepsilon}{\varepsilon'} \approx \frac{\bar{\varepsilon}}{\varepsilon'} [1 + \frac{(\delta\varepsilon)^2}{\varepsilon \bar{\varepsilon}'}]$ . In the following derivation the second-order correction is neglected. Moreover, for reasons of simplicity, the average energy  $\bar{\varepsilon}$  is replaced from now on by  $\varepsilon$ . Since the trajectory presented in Sec. II is given in terms of the proper time  $\tau$ , we change the integration variable in Eq. (31), leading to

$$\mathcal{T}_\mu(k') = \int_{-\infty}^{\infty} d\tau \frac{P_\mu(\tau)}{m} e^{i\psi}, \quad (33)$$

where the relation between  $P_\mu$  and  $dx_\mu/d\tau$  was used. With the substitution of the trajectory (28) and the emitted photon wave vector (32) into expression (33), the phase reads

$$\psi = \psi_I \tau - z_{11} \sin \phi_1 - z_{12} \cos \phi_1 - z_{21} \sin \phi_2 - z_{22} \cos \phi_2 - z_3^\pm \sin(\phi_1 \pm \phi_2), \quad (34)$$

where + and - correspond to the counterrotating and corotating cases, respectively. For further simplification the following quantities were introduced:

$$\begin{aligned} z_{11} &= -\frac{um\xi_1}{\omega_1} \left[ -n_x + \frac{p_x \omega}{\varepsilon \omega_1} (1 - n_z) \right], & z_{12} &= -\frac{um\xi_1 \varepsilon_1}{\omega_1} n_y, \\ z_3^+ &= -\frac{u\omega m^2 \xi_1 \xi_2 \varepsilon_+}{\varepsilon(\omega_1 + \omega_2)^2}, & z_3^- &= \frac{u\omega m^2 \xi_1 \xi_2 \varepsilon_- n_z}{\varepsilon(\omega_1 - \omega_2)^2}, \\ z_{21} &= -\frac{um\xi_2}{\omega_2} \left[ -n_x + \frac{p_x \omega}{\varepsilon \omega_2} (1 + n_z) \right], & z_{22} &= -\frac{um\xi_2 \varepsilon_2}{\omega_2} n_y, \end{aligned} \quad (35)$$

with  $u \equiv \omega' / (\varepsilon - \omega')$ . By utilizing the definitions

$$z_1 = \sqrt{z_{11}^2 + z_{12}^2}, \quad z_2 = \sqrt{z_{21}^2 + z_{22}^2}, \quad (36)$$

$$\varphi_1 = \tan^{-1} \left( \frac{z_{12}}{z_{11}} \right), \quad \varphi_2 = \tan^{-1} \left( \frac{z_{22}}{z_{21}} \right), \quad (37)$$

the phase can be simplified even more to

$$\begin{aligned} \psi &= \psi_l \tau - z_1 \sin(\phi_1 - \varphi_1) - z_2 \sin(\phi_1 - \varphi_1) \\ &\quad - z_3^\pm \sin(\phi_1 \pm \phi_2). \end{aligned} \quad (38)$$

The linear term in the phase has the coefficient

$$\psi_l = \frac{\varepsilon^2 u}{m} (1 - v_x n_x - v_z n_z), \quad (39)$$

with  $v_x = p_x/\varepsilon$  and  $v_z = \bar{P}_z/\varepsilon$  being the average velocities along the  $x$  and  $z$  directions. Substituting Eq. (38) as well as Eq. (27) into Eq. (33) and using the Jacobi-Anger expansion for the Bessel function, we can obtain the transition amplitudes after some tedious, but straightforward, derivations:

$$\mathcal{T}_\mu = 2\pi \sum_{s_1, s_2, s_3} \mathcal{M}_\mu(s_1, s_2, s_3) \delta(\Omega_{s_1, s_2, s_3}), \quad (40)$$

$$\mathcal{M}_0 = \sum_{s_3} \left[ \left( \frac{\varepsilon}{m} B_0(\mathbf{3}) + \frac{\varepsilon_+ \omega m \xi_1 \xi_2}{\varepsilon(\omega_1 + \omega_2)} B_1(\mathbf{3}) \right) B_0(\mathbf{1}) B_0(\mathbf{2}) + p_x \omega \left( \frac{\xi_1}{\varepsilon \omega_1} B_1(\mathbf{1}) B_0(\mathbf{2}) + \frac{\xi_2}{\varepsilon \omega_2} B_0(\mathbf{1}) B_1(\mathbf{2}) \right) B_0(\mathbf{3}) \right], \quad (43)$$

$$\mathcal{M}_1 = \sum_{s_3} \left[ \frac{p_x}{m} B_0(\mathbf{1}) B_0(\mathbf{2}) B_0(\mathbf{3}) + [\xi_1 B_0(\mathbf{2}) B_1(\mathbf{1}) + \xi_2 B_0(\mathbf{1}) B_1(\mathbf{2}) B_0(\mathbf{3})] \right], \quad (44)$$

$$\mathcal{M}_2 = \sum_{s_3} [\xi_1 \varepsilon_1 B_0(\mathbf{2}) B_2(\mathbf{1}) + \xi_2 \varepsilon_2 B_0(\mathbf{1}) B_2(\mathbf{2})] B_0(\mathbf{3}), \quad (45)$$

$$\mathcal{M}_3 = \sum_{s_3} \left[ \left( \frac{\bar{P}_z}{m} B_0(\mathbf{3}) - \frac{\varepsilon_- \omega m \xi_1 \xi_2}{\varepsilon(\omega_1 - \omega_2)} B_1(\mathbf{3}) \right) B_0(\mathbf{1}) B_0(\mathbf{2}) + p_x \omega \left( \frac{\xi_1}{\varepsilon \omega_1} B_1(\mathbf{1}) B_0(\mathbf{2}) - \frac{\xi_2}{\varepsilon \omega_2} B_0(\mathbf{1}) B_1(\mathbf{2}) \right) B_0(\mathbf{3}) \right]. \quad (46)$$

Here, we have  $\mathbf{1} \equiv (s_1, z_1, \varphi_1)$ ,  $\mathbf{2} \equiv (s_2, z_2, \varphi_2)$ , and  $\mathbf{3} \equiv (s_3, z_3, 0)$ . In the derivation, we consider the identities used in Ref. [65],

$$(1, \cos \phi, \sin \phi) e^{-z \sin(\phi - \varphi)} = \sum_s (B_0, B_1, B_2) e^{-is\phi}. \quad (47)$$

The functions  $B_0$ ,  $B_1$ , and  $B_2$  are related to the Bessel function  $J_s(z)$  and its first derivative  $J'_s(z)$  through

$$B_0(s, z, \varphi) = J_s(z) e^{is\varphi}, \quad (48)$$

$$B_1(s, z, \varphi) = \left[ \frac{s}{z} J_s(z) \cos \varphi - i J'_s(z) \sin \varphi \right] e^{is\varphi}, \quad (49)$$

$$B_2(s, z, \varphi) = \left[ \frac{s}{z} J_s(z) \sin \varphi + i J'_s(z) \cos \varphi \right] e^{is\varphi}. \quad (50)$$

Finally, the emitted intensity may be obtained by integrating (30) over the polar angle:

$$\frac{dI}{d\omega' d\varphi} = \frac{\alpha m}{2\pi \varepsilon'} \int d(\cos \theta) \omega'^2 \sum_{s_L, s_R} |\mathcal{M}_\mu(s_L, s_R)|^2 \delta(\Omega_{s_L, s_R}), \quad (51)$$

where the identity  $\delta^2(\Omega_{s_L, s_R}) = \frac{\tau_0}{2\pi} \delta(\Omega_{s_L, s_R})$  has been used. The proper interaction time is given by  $\tau_0 = (m/\varepsilon) T_0$ . As squaring  $\mathcal{T}$  does not mix terms associated with different  $s_L$  and  $s_R$  indices, the interference takes place only between terms included within  $\mathcal{M}_\mu(s_L, s_R)$ . The condition imposed by the

where the  $\delta$  function argument is given by

$$\Omega_{s_1, s_2, s_3} \equiv \psi_l - \frac{\varepsilon}{m} [(s_1 + s_3)\omega_1 + (s_2 \pm s_3)\omega_2], \quad (41)$$

with  $+$  and  $-$  in the last term representing the counterrotating and the corotating cases, respectively. One may notice that different combinations of the indices  $s_1$ ,  $s_2$ , and  $s_3$  may yield the same  $\delta$  function argument. As a result, when  $\mathcal{T}$  is squared, interference terms will arise which depend on the quantity  $\omega_2/\omega_1$ . If this ratio is an integer, the motion is periodic with the frequency  $2\pi/\omega_1$ . Otherwise, the motion is nonperiodic. Because the periodic motion is not easily fulfilled in reality, we will focus on the nonperiodic motion below.

By defining  $s_R \equiv s_1 + s_3$  and  $s_L \equiv s_2 \pm s_3$ , one may write

$$\mathcal{T}_\mu = 2\pi \sum_{s_L, s_R} \mathcal{M}_\mu(s_L, s_R) \delta(\Omega_{s_L, s_R}), \quad (42)$$

with  $\Omega_{s_R, s_L} \equiv \psi_l - \varepsilon/m(s_R\omega_1 + s_L\omega_2)$ . The matrix elements take the form

$\delta$  function, namely,  $\Omega_{s_L, s_R} = 0$ , illustrates the energy conservation in the radiation process and determines the relation between  $\cos \theta$  and  $\omega'$  and  $\varphi$ ,

$$1 - \rho - \bar{v}_z \cos \theta = \bar{v}_x \cos \varphi \sqrt{1 - \cos^2 \theta}. \quad (52)$$

By squaring and solving this equation one obtains two possible angles,

$$\cos \theta_\pm = \frac{\bar{v}_z(1 - \rho) \pm \bar{v}_x \cos \varphi \sqrt{\Delta}}{\bar{v}_z^2 + \bar{v}_x^2 \cos^2 \varphi}, \quad (53)$$

where the following quantities are introduced:

$$\Delta \equiv \bar{v}_z^2 + \bar{v}_x^2 \cos^2 \varphi - (1 - \rho)^2, \quad (54)$$

$$\rho \equiv \frac{(s_R \omega_1 + s_L \omega_2)}{u \varepsilon}. \quad (55)$$

Note that, here,  $\pm$  just represents different solutions for  $\cos \theta$  and does not relate to the co- or counterrotating cases. When (52) is squared, a redundant solution is added, which solves an equation similar to Eq. (52), but with a minus sign on the left side. Thus, the solutions given in (53) are physical only if, when they are substituted into the left-hand side of (52), a positive result follows. A solution that does not meet this criterion is therefore excluded. Physically, this exclusion ensures that the emission is along the electron's direction of propagation.

Employing the  $\delta$  function to perform the integration leads to

$$\frac{dI}{d\omega'd\varphi} = \frac{\alpha\varepsilon\omega'^2}{2\pi\varepsilon'm} \sum_{i=\pm} \sum_{s_L, s_R} |\mathcal{M}_\mu(s_L, s_R)|^2 \left| \frac{d\Omega_{s_L, s_R}}{d(\cos\theta)} \right|_{\theta=\theta_i}^{-1}. \quad (56)$$

The reciprocal of the derivative of the  $\delta$  function, required for the integration, reads

$$\left| \frac{d\Omega_{s_L, s_R}}{d(\cos\theta)} \right|^{-1} = \frac{m}{\varepsilon^2 u} \left| \frac{1}{\bar{v}_x \cos\varphi \cot\theta - \bar{v}_z} \right| \equiv \kappa(\theta). \quad (57)$$

Substituting (57) into (56) yields the final result

$$\frac{dI}{d\omega'd\varphi} = \frac{\alpha\omega'^2}{2\pi\varepsilon\varepsilon'} \sum_{i=\pm} \sum_{s_L, s_R} |\mathcal{M}_\mu(s_L, s_R)|^2 \kappa(\theta_i). \quad (58)$$

Here,  $i = \pm$  represent the two solutions for  $\cos\theta$  in Eq. (53).

For a spinor particle the initial emission expression (30) is modified as follows:

$$|\mathcal{T}|^2 \rightarrow |\mathcal{K}|^2 \equiv -\left(\frac{\varepsilon'^2 + \varepsilon^2}{2\varepsilon\varepsilon'}\right) |\mathcal{T}_\mu|^2 + \frac{\omega'^2}{2\varepsilon'^2\varepsilon^2} |\mathcal{T}_0|^2. \quad (59)$$

Therefore, the final results for a spin- $\frac{1}{2}$  particle are obtained:

$$\frac{dI}{d\omega'd\varphi} = \frac{\alpha m \omega'^2}{2\pi\varepsilon} \sum_{i=\pm} \sum_{s_L, s_R} \kappa(\theta_i) \left[ -\left(\frac{\varepsilon'^2 + \varepsilon^2}{2\varepsilon\varepsilon'}\right) |\mathcal{M}_\mu(s_L, s_R)|^2 + \frac{\omega'^2}{2\varepsilon'^2\varepsilon^2} |\mathcal{M}_0(s_L, s_R)|^2 \right]. \quad (60)$$

In the derivation above, we include only the linear dependence on  $\tau$  for phases  $\phi_1$  and  $\phi_2$  in the classical momentum (27) and trajectory (28) and ignore the higher-order corrections. From Eqs. (22) and (23), we can see that the next order corrections are oscillations with an amplitude of  $C_1, C_2, C_{1-2}$ , and  $C_{1+2}$  in Eq. (24). The difference between the co- and counterrotating cases is  $C_{1-2}$  and  $C_{1+2}$ , which have the same order of magnitude. Therefore, by following the same procedure as in the previous work in [64], we can infer the same validity conditions for the matrix elements in Eqs. (43)–(46); see Eq. (111) in Ref. [64].

## B. Numerical results

In the following we present typical spectra for an ultrarelativistic electron in the strong-field regime ( $\xi_1 \gg 1$ ), and we will focus on the influence of the sense of rotation of the laser fields on the electron's radiation spectra. We know that the quantum parameter  $\chi = e\sqrt{-(F^{\mu\nu}P_\nu)^2}/m^3$  can totally characterize the radiation property if the LCFA is applied, but in a general field configuration where the LCFA may not be fully valid,  $\chi$  can still characterize some aspects of the radiation. From a previous study [22] we know that there are three different regimes where the radiation behavior changes dramatically. Therefore, we will also investigate the influence of the corotating and counterrotating laser beams on the radiation spectra in these three regimes. In order to distinguish the different regimes, we also define  $\chi_{1,2} \equiv \xi_{1,2} k_{1,2} \cdot \bar{P}/m^2$  as the quantum parameters for the  $\xi_1$  and  $\xi_2$  lasers, respectively.

From Eqs. (43)–(46) for the matrix elements, we can see that the differences between the corotating and counterrotating cases appear in four places:

(i) The crossing term in  $\mathcal{M}_\mu$ , proportional to  $\xi_1\xi_2$ , moves from  $\mathcal{M}_3$  in the corotating case to  $\mathcal{M}_0$  in the counterrotating case. This is because of the crossing term in the classical four-momentum appearing in energy for the corotating case while appearing in  $P_z$  for the counterrotating case [see Eq. (27)].

(ii) Two terms in  $\mathcal{M}_2$  show a different sign with respect to each other in the counterrotating case. This is related to the oscillations in  $P_y$  changing their direction between co- and counterrotating cases.

(iii) One of the arguments for the Bessel function  $z_3^\pm$  in Eq. (35) shows a difference between the two cases. The reason is again due to the crossing term in the four-momentum since this term has different prefactors in the co- and counterrotating cases.

(iv) For the Bessel function with the argument  $z_2$  the order also changes between the two cases. From Eq. (41), we can see that  $s_R$  and  $s_L$  are the same for both cases when the emitted photon  $k'_\mu$  is fixed. However,  $s_L = s_2 \pm s_3$  depends on  $s_2$  and  $s_3$  differently for the co- and counterrotating cases, which changes the physical meaning of  $s_3$ . In the corotating case  $s_3$  represents the process of absorbing a certain number of photons from one laser and then emitting the same number to the other laser, while in the counterrotating case  $s_3$  corresponds to either absorbing from or emitting to both lasers the same number of photons at one time, depending on  $s_3$  being positive or negative.

From Eqs. (43)–(46), we can see that the terms proportional to the transverse momentum  $p_x$  are the same for both the corotating and counterrotating cases and will not contribute to the dissimilarities between the two cases. Therefore, we choose  $p_x = 0$  in the following calculations, but the conclusion is the same for  $p_x \neq 0$ . Moreover, when  $p_x = 0$ , the validity conditions for the matrix elements will be fulfilled automatically [64].

In regime I ( $\chi_1 \gg \chi_2$ ), the  $\xi_1$  laser will dominate the radiation process. The major task in calculating the spectrum is to evaluate the Bessel functions in the matrix elements. We know that  $J_n(z)$  will vanish if its order  $n$  is larger enough than the argument  $z$ . Therefore, it is wise to estimate the maximum value of the Bessel function's argument before calculating the matrix elements. For this purpose Fig. 4 illustrates the behavior of said arguments and  $\cos(\theta)$  depending on  $s_R$ . It shows that arguments  $z_1$  and  $z_2$  and the angle  $\theta$  are the same for both cases, as expected. The only difference lies in  $z_3$ , which depends on the emission angle in the corotating case but is a constant in the counterrotating case [see also Eq. (35)].

Because  $\xi_1 = 200$  and  $\varepsilon = 767m$  in the calculation,  $z_1$  is rather large and increases with the emission angle. However, from the two panels in the first row of Fig. 4, we can see that there is a certain region (between the two vertical dashed lines in the plots) when  $z_1 \sim s_1$  and the contribution from  $J_{s_1}(z_1)$  in the matrix elements is not negligible. Please note that  $s_1 = s_R - s_3$  and  $s_3$  is usually much smaller than  $s_R$  as  $z_3 \ll z_1$ . In this region,  $\cos\theta$  is around 0.965, which coincides with the propagation direction of the electron  $P_z/\varepsilon \approx 0.9654$ , as expected.

For the third row in Fig. 4, we can see that  $z_2$  is the same for both the co- and counterrotating cases. However,  $s_2$  is different between the two cases, as mentioned before. Naturally, now the question arises of whether this difference in  $s_2$  will lead to



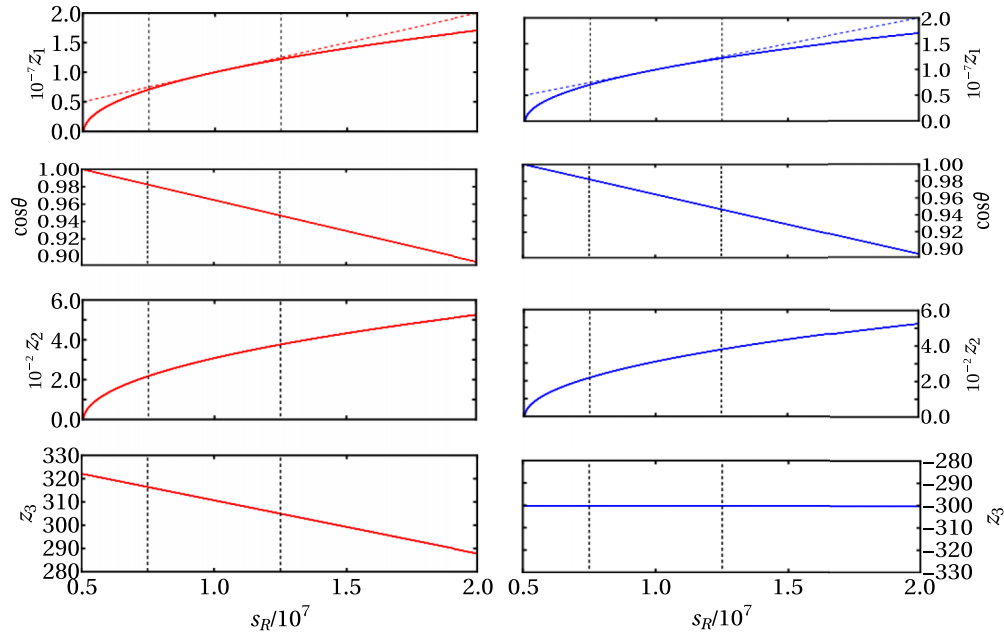


FIG. 4. The emission direction  $\cos \theta$  and the arguments of the Bessel function  $z_1$ ,  $z_2$ , and  $z_3$  as a function of  $s_R$ . The left column (red lines) shows the corotating case, while the right one (blue lines) shows the counterrotating case. Here,  $\xi_1 = 200$ ,  $\xi_2 = 0.35$ , and the average energy  $\varepsilon = 767m$ , which corresponds to  $\chi_1/\chi_2 = 10$ . The emitted photon energy  $\omega'$  is chosen to correspond to  $u = 0.02$ . The dashed lines in the first row correspond to  $z_1 = s_R$ .

a difference in spectra. Our conjecture is no because the sum over  $s_3$  in Eqs. (43)–(46) will cover the whole region within which  $J_{s_2}(z_2)$  is not negligible. The only effect will be the peak of the harmonic in the spectrum perhaps being shifted when the harmonic structure is obvious.

From Eq. (35) we can estimate that in the relevant region  $z_3^-$  and  $z_3^+$  will have similar amplitudes in the co- and counterrotating cases (see also the fourth row of Fig. 4), despite  $z_3^-$  depending on the direction of emission. The different signs between  $z_3^-$  and  $z_3^+$  will not play a major role when summing over  $s_3$ , and only a quantitative difference may appear in the spectra.

To test our above conjectures, the spectra for both the co- and counterrotating cases are displayed in Fig. 5. From Fig. 5(a), we can see that the spectra for both cases have, indeed, exactly the same shape, and the difference is almost invisible. Only if we zoom in can we see that the corotating case gives slightly larger values than the counterrotating one. More interestingly, the LCFA formula [65] predicts almost the same spectrum for both cases (see the zoomed-in scale). The relative difference would be very large at the beginning because the harmonic structure at low energies cannot be reproduced by the LCFA [16].

The relative difference between accurate spectra for the corotating case and for the counterrotating case is shown in Fig. 5(b), where the relative difference of the accurate spectra is less than 3% in the main part of the spectrum. This small difference can be explained by looking at the quantum parameter  $\chi$  in Fig. 6. From Fig. 6 we can see that  $\chi$  has similar average values for both the co- and counterrotating setups and therefore gives almost the same results for both cases. The general behavior of  $\chi$  can be estimated by the well-known formula  $\chi \approx |d\mathbf{P}/d\tau|/m^2$ ; the small difference between the

co- and counterrotating cases, however, is due to higher-order corrections that are not included in this estimation.

This small difference also means that differences (i) and (ii) mentioned before also do not cause a big deviation between

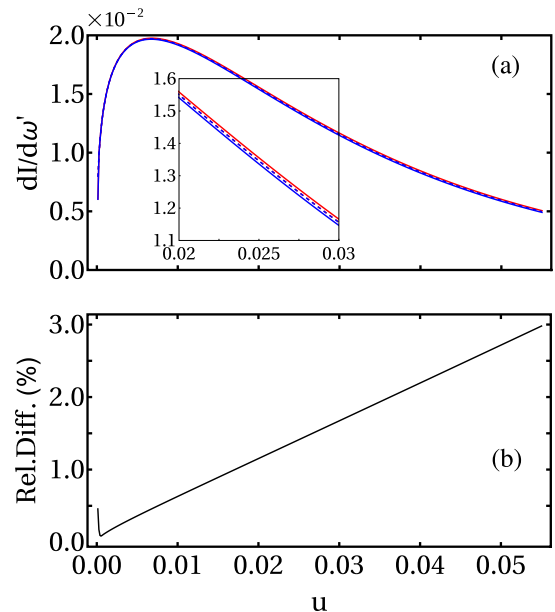


FIG. 5. (a) The radiation spectra as a function of  $u$  for both the corotating case (red) and the counterrotating case (blue). The inset is a zoom of  $0.02 < u < 0.03$ . The solid curves are the results based on Eq. (60), and the dashed lines are the prediction of the LCFA. (b) The relative difference between the accurate results (solid lines) and the LCFA predictions (dashed lines). The parameters for the laser beams and the electron are the same as in Fig. 4.

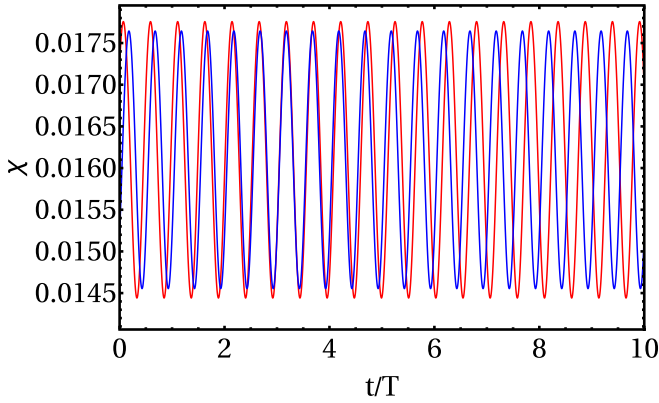


FIG. 6. The quantum parameter  $\chi$  for both the co- and counterrotating (red and blue lines) cases as a function of time. All the parameters are the same as in Fig. 5.

the co- and counterrotating cases. The reason is that when we calculate  $|\mathcal{M}_\mu|^2 = |\mathcal{M}_0|^2 - |\mathcal{M}_1|^2 - |\mathcal{M}_2|^2 - |\mathcal{M}_3|^2$  in Eq. (60), the differences that appear in  $\mathcal{M}_0$ ,  $\mathcal{M}_2$ , and  $\mathcal{M}_3$  will contribute to the same degree in both cases. For example, in the corotating case, the crossing term in  $\mathcal{M}_3$  and the second term in  $\mathcal{M}_2$  have the same sign in the final expression in Eq. (60). In the counterrotating case, on the other hand, the crossing term moves to  $\mathcal{M}_0$ , and the second term in  $\mathcal{M}_2$  changes sign. Hence, in the end they will make a similar contribution to the corotating case. Moreover, the contribution is independent of the emitted photon energy because there is no obvious harmonic structure in the spectrum in this regime. This leads to the linear increase in the relative difference with respect to the emitted photon energy in Fig. 5(b) since the prefactor in Eq. (60) is proportional to  $\omega'$ .

For regime II ( $\chi_1 \sim \chi_2$ ), the two lasers will both play a role in the radiation spectra. In Fig. 7(a), we show the accurate

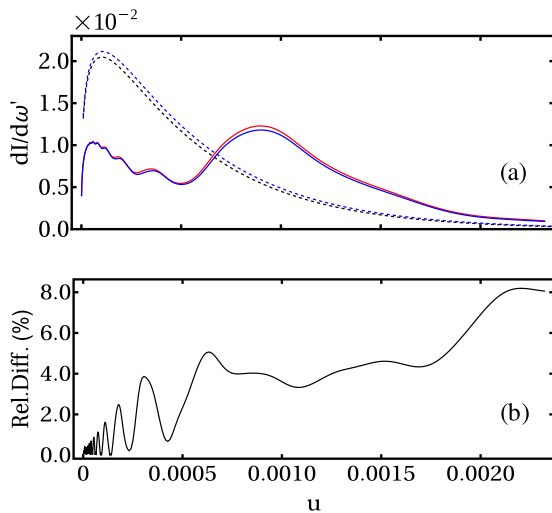


FIG. 7. (a) The radiation spectra as a function of  $u$  for both the corotating case (red line) and the counterrotating case (blue lines). (b) The relative difference between the two accurate spectra in (a). Here,  $\xi_1 = 20$ ,  $\xi_2 = 0.35$ , and the average energy  $\varepsilon = 108m$ , which corresponds to  $\chi_1/\chi_2 = 0.5$ .

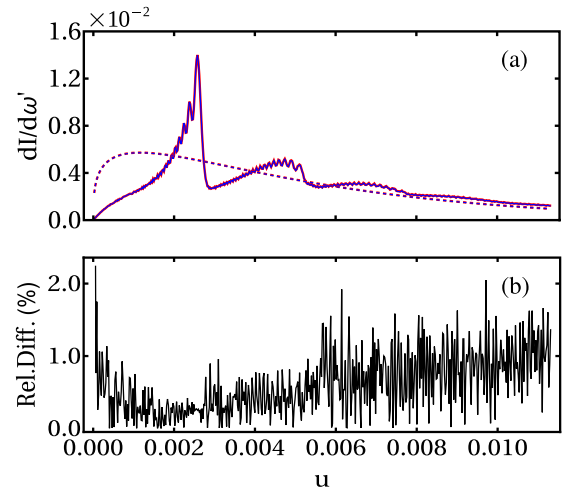


FIG. 8. (a) The radiation spectra as a function of  $u$  for both the corotating case (red lines) and the counterrotating case (blue lines). (b) The relative difference between the two accurate spectra in (a). Here,  $\xi_1 = 20$ ,  $\xi_2 = 1$ , and the average energy  $\varepsilon = 447m$ , which corresponds to  $\chi_1/\chi_2 = 0.01$ .

spectra for the co- and counterrotating cases with  $\chi_1/\chi_2 = 0.5$  as well as the LCFA predictions. First of all, we note that the spectra based on the BK method and LCFA are quite different. This is because both lasers contribute to the radiation process and the interference effect caused by  $\xi_2 = 0.35$  is not negligible. The second peak in the BK spectra is caused by the contributions from the  $\xi_2$  laser as the position of this peak roughly corresponds to the first harmonic of the  $\xi_2$  laser with  $u \approx 4\varepsilon^2\omega/(m^2\varepsilon - 4\varepsilon^2\omega) = 0.0094$ . The two BK spectra again have a similar shape; however, it is clearly visible that the deviation between the two spectra is more prominent than in regime I.

The relative difference between the co- and counterrotating spectra based on the BK method is displayed in Fig. 7(b). As opposed to regime I, the relative difference here is not linear in  $u$  and oscillates. The reason is that with the present parameters the harmonic structure starts to become visible in the spectrum, and therefore, difference (iv) will modify the position of the harmonics. For example, the position of the harmonics around  $u = 0.00035$  differs by  $0.001m$  between the two cases. However, the main harmonics around  $u = 0.001$  are in the same place since this harmonic is mainly a consequence of  $\xi_2$ .

For regime III ( $\chi_1 \ll \chi_2$ ), the radiation will now be dominated by the  $\xi_2$  laser, and therefore, the LCFA predictions give totally different spectra. From Fig. 8(a), we see that the main structure of the spectra consists of the harmonics created by  $\xi_2$ . The additional fast oscillation is the modification from  $\xi_1$ . Like in the previous two regimes, the spectra for both cases are the same and the relative difference between them in Fig. 8(b) is less than 1%. This is because in the single-laser case, the change in the sense of rotation will not affect the radiation process. Please note that there are two solid lines on top of each other in Fig. 8(a).

The fast oscillation in the relative difference is due to the harmonics being shifted by different  $s_2$  for the co- and counterrotating cases [difference (iv)]. However, the main

peak of the spectrum is at the same position because it originates mainly from the  $\xi_2$  laser. Moreover, the average relative difference also increases approximately linearly for a large photon energy, which is due to the spectrum behaving like the predictions of the LCFA at large emitted energies.

Upon comparison, the relative differences in regimes I, II, and III appear larger in regime II but smaller in regimes I and III. This is a consequence of the system for  $\chi_1 \ll \chi_2$  or  $\chi_1 \gg \chi_2$  approaching the rotationally symmetric single-laser case in which the change in the rotational sense will not affect the spectrum noticeably. For  $\chi_1 \sim \chi_2$ , on the other hand, both lasers contribute to the radiation, and changing the laser's sense of rotation will induce a more significant alteration of the spectrum. However, the spectrum does not change shape since the change in rotational direction has no effect on the characteristic timescale. To understand this similarity, we can go back to the original formula for the Baier-Katkov integral in Eq. (31), where the velocity of the electron plays a major role. Here, the velocities for both cases are similar since the crossing term in Eq. (27) is second order in magnitude. More intuitively, we know that for an ultrarelativistic electron in a strong background field the emission is mainly along the propagation direction within the  $1/\gamma$  cone and the shape of the spectrum is determined by the electron dynamics in this region, which can be characterized by a timescale defined as  $t_c := |\dot{\mathbf{v}}|/|\ddot{\mathbf{v}}|$ , with  $\mathbf{v}$  being the electron's velocity in the fields. Based on the momentum in Eq. (27),  $t_c$  is similar for both cases despite the crossing term moving from  $P_z$  in the corotating case to  $\varepsilon$  in the counterrotating one.

#### IV. CONCLUSIONS

In this paper the dynamics of an ultrarelativistic electron in counterpropagating laser beams with a variable sense of rotation were explored. The classical momentum and trajectory were analytically derived assuming that the particle's averaged energy is the dominant factor while the transverse momentum is small compared to the total energy. The difference between the classical momentum for both co- and counterrotating laser-beam arrangements was investigated. The main difference appeared to be the crossing term related to both laser beams which moves from  $P_z$  in the corotating case to the total energy  $\varepsilon$  in the counterrotating case [see

Eqs. (17) and (19)]. This means that for a vanishing initial transverse momentum the electron in a counterrotating setup has a constant velocity in the  $z$  direction. And if we change to the electron's rest frame, the electron's trajectory is almost the same as in a two-color rotating electric-field configuration, which is a widely used model for analyzing the so-called dynamically assisted Schwinger effect [51,66–72]. Therefore, the counterrotating setup can provide a mapping of this simple model for the whole region rather than only a small vicinity around the antinode of a standing wave, where the rotating electric field can be realized. Moreover, a comparison with the full numerical solution was carried out, resulting in good agreement and validation of our analytical solution within the given conditions.

The closed formula of the analytical approximation for the classical electron dynamics allows one to calculate the rates of the quantum processes in strong CPW background fields by employing the Baier-Katkov semiclassical operator method. In this formalism, while the electron dynamics in the background classical fields are accounted for quasiclassically, the photon emission is treated quantum mechanically, fully taking into account the quantum recoil of the emitted photon. The Baier-Katkov integrals were analytically solved, yielding closed formulas in terms of various Bessel functions. Different expressions were obtained for the corotating and counterrotating cases. The results were employed to compare the corotating and counterrotating cases in detail. We observed that even though the classical dynamics show a qualitative difference between the two cases, the emitted spectra all have the same shape for two cases in different parameter regimes with a relative difference of only a few percent. To understand these deviations, we analyzed the arguments of the Bessel functions in the matrix elements in detail. The influence of the rotational direction is prominent only when the radiation process is dominated by both laser beams.

#### ACKNOWLEDGMENTS

L.A. would like to thank the group of Prof. C. H. Keitel for the nice hospitality at MPIK in Heidelberg. The authors would like to thank Dr. E. Raicher and Dr. K. Z. Hatsagortsyan for helpful discussions during the project and also for reading the manuscript, as well as their useful comments concerning it.

- 
- [1] The Vulcan facility, <https://www.clf.stfc.ac.uk/Pages/Vulcan-laser.aspx>.
  - [2] J. W. Yoon, C. Jeon, J. Shin, S. K. Lee, H. W. Lee, I. W. Choi, H. T. Kim, J. H. Sung, and C. H. Nam, Achieving the laser intensity of  $5.5 \times 10^{22}$  W/cm<sup>2</sup> with a wavefront-corrected multi-PW laser, *Opt. Express* **27**, 020412 (2019).
  - [3] The Extreme Light Infrastructure (ELI), <http://www.eli-laser.eu/>.
  - [4] Exawatt Center for Extreme Light Studies (XCELS), <http://www.xcels.iapras.ru/>.
  - [5] M. Marklund and P. K. Shukla, Nonlinear collective effects in photon-photon and photon-plasma interactions, *Rev. Mod. Phys.* **78**, 591 (2006).
  - [6] A. Di Piazza, C. Müller, K. Z. Hatsagortsyan, and C. H. Keitel, Extremely high-intensity laser interactions with fundamental quantum systems, *Rev. Mod. Phys.* **84**, 1177 (2012).
  - [7] T. Heinzl, Strong-field QED and high-power lasers, *Int. J. Mod. Phys. A* **27**, 1260010 (2012).
  - [8] G. V. Dunne, Extreme quantum field theory and particle physics with IZEST, *Eur. Phys. J. Spec. Top.* **223**, 1055 (2014).
  - [9] I. C. E. Turcu, B. Shen, D. Neely, G. Sarri, K. A. Tanaka, P. McKenna, S. P. D. Mangles, T.-P. Yu, W. Luo, X.-L. Zhu, and Y. Yin, Quantum electrodynamics experiments with colliding petawatt laser pulses, *High Power Laser Sci. Eng.* **7**, e10 (2019).

- [10] A. Gonoskov, T. G. Blackburn, M. Marklund, and S. S. Bulanov, Charged particle motion and radiation in strong electromagnetic fields, *Rev. Mod. Phys.* **94**, 045001 (2022).
- [11] A. Fedotov, A. Ilderton, F. Karbstein, B. King, D. Seipt, H. Taya, and G. Torgrimsson, Advances in QED with intense background fields, *Phys. Rep.* **1010**, 1 (2023).
- [12] J. M. Cole *et al.*, Experimental evidence of radiation reaction in the collision of a high-intensity laser pulse with a laser-wakefield accelerated electron beam, *Phys. Rev. X* **8**, 011020 (2018).
- [13] K. Poder *et al.*, Experimental signatures of the quantum nature of radiation reaction in the field of an ultraintense laser, *Phys. Rev. X* **8**, 031004 (2018).
- [14] W. H. Furry, On bound states and scattering in positron theory, *Phys. Rev.* **81**, 115 (1951).
- [15] V. G. Bagrov and D. Gitman, *Mathematics and its Applications: Exact Solutions of Relativistic Wave Equations*, Vol. 39 (Springer, Berlin, 1990).
- [16] C. N. Harvey, A. Ilderton, and B. King, Testing numerical implementations of strong-field electrodynamics, *Phys. Rev. A* **91**, 013822 (2015).
- [17] A. DiPiazza, M. Tamburini, S. Meuren, and C. H. Keitel, Implementing nonlinear Compton scattering beyond the local-constant-field approximation, *Phys. Rev. A* **98**, 012134 (2018).
- [18] A. DiPiazza, M. Tamburini, S. Meuren, and C. H. Keitel, Improved local-constant-field approximation for strong-field QED codes, *Phys. Rev. A* **99**, 022125 (2019).
- [19] A. Ilderton, B. King, and D. Seipt, Extended locally constant field approximation for nonlinear Compton scattering, *Phys. Rev. A* **99**, 042121 (2019).
- [20] A. Ilderton, B. King, and A. J. MacLeod, Absorption cross section in an intense plane wave background, *Phys. Rev. D* **100**, 076002 (2019).
- [21] T. Podszus and A. Di Piazza, High-energy behavior of strong-field QED in an intense plane wave, *Phys. Rev. D* **99**, 076004 (2019).
- [22] Q. Z. Lv, E. Raicher, C. H. Keitel, and K. Z. Hatsagortsyan, Anomalous violation of the local constant field approximation in colliding laser beams, *Phys. Rev. Res.* **3**, 013214 (2021).
- [23] A. Ilderton, Note on the conjectured breakdown of QED perturbation theory in strong fields, *Phys. Rev. D* **99**, 085002 (2019).
- [24] V. Popov, V. Mur, and B. Karnakov, The imaginary-time method for relativistic problems, *JETP Lett.* **66**, 229 (1997).
- [25] J. I. Gersten and M. H. Mittleman, Eikonal theory of charged-particle scattering in the presence of a strong electromagnetic wave, *Phys. Rev. A* **12**, 1840 (1975).
- [26] G. R. Mocken, M. Ruf, C. Müller, and C. H. Keitel, Nonperturbative multiphoton electron-positron-pair creation in laser fields, *Phys. Rev. A* **81**, 022122 (2010).
- [27] A. Di Piazza, Ultrarelativistic electron states in a general background electromagnetic field, *Phys. Rev. Lett.* **113**, 040402 (2014).
- [28] A. Di Piazza, Analytical tools for investigating strong-field qed processes in tightly focused laser fields, *Phys. Rev. A* **91**, 042118 (2015).
- [29] A. Di Piazza, Nonlinear Breit-Wheeler pair production in a tightly focused laser beam, *Phys. Rev. Lett.* **117**, 213201 (2016).
- [30] A. Di Piazza, First-order strong-field QED processes in a tightly focused laser beam, *Phys. Rev. A* **95**, 032121 (2017).
- [31] V. N. Baier and V. M. Katkov, *Sov. Phys. JETP* **26**, 854 (1968).
- [32] V. N. Baier, V. M. Katkov, and V. M. Strakhovenko, *Electromagnetic Processes at High Energies in Oriented Single Crystals* (World Scientific, Singapore, 1994).
- [33] V. B. Berestetskii, E. M. Lifshitz, and L. P. Pitevsikii, *Quantum Electrodynamics* (Pergamon, Oxford, 1982).
- [34] S. S. Bulanov, V. D. Mur, N. B. Narozhny, J. Nees, and V. S. Popov, Multiple colliding electromagnetic pulses: A way to lower the threshold of  $e^+e^-$  pair production from vacuum, *Phys. Rev. Lett.* **104**, 220404 (2010).
- [35] J. Magnusson, A. Gonoskov, M. Marklund, T. Z. Esirkepov, J. K. Koga, K. Kondo, M. Kando, S. V. Bulanov, G. Korn, C. G. R. Geddes, C. B. Schroeder, E. Esarey, and S. S. Bulanov, Multiple colliding laser pulses as a basis for studying high-field high-energy physics, *Phys. Rev. A* **100**, 063404 (2019).
- [36] A. Golla, B. Chalopin, M. Bader, I. Harder, K. Mantel, R. Maiwald, N. Lindlein, M. Söndermann, and G. Leuchs, Generation of a wave packet tailored to efficient free space excitation of a single atom, *Eur. Phys. J. D* **66**, 190 (2012).
- [37] I. Gonoskov, A. Aiello, S. Heugel, and G. Leuchs, Dipole pulse theory: Maximizing the field amplitude from  $4\pi$  focused laser pulses, *Phys. Rev. A* **86**, 053836 (2012).
- [38] A. V. Bashinov, A. A. Gonoskov, A. V. Kim, M. Marklund, G. Mourou, and A. M. Sergeev, Electron acceleration and emission in a field of a plane and converging dipole wave of relativistic amplitudes with the radiation reaction force taken into account, *Quantum Electron.* **43**, 291 (2013).
- [39] A. V. Bashinov, P. Kumar, and E. S. Efimenko, Confinement of electrons in the focus of the dipole wave, *Quantum Electron.* **49**, 314 (2019).
- [40] J. G. Kirk, A. R. Bell, and I. Arka, Pair production in counter-propagating laser beams, *Plasma Phys. Control. Fusion* **51**, 085008 (2009).
- [41] S. S. Bulanov, T. Z. Esirkepov, A. G. R. Thomas, J. K. Koga, and S. V. Bulanov, Schwinger limit attainability with extreme power lasers, *Phys. Rev. Lett.* **105**, 220407 (2010).
- [42] A. Gonoskov, A. Bashinov, I. Gonoskov, C. Harvey, A. Ilderton, A. Kim, M. Marklund, G. Mourou, and A. Sergeev, Anomalous radiative trapping in laser fields of extreme intensity, *Phys. Rev. Lett.* **113**, 014801 (2014).
- [43] Z. Gong, R. H. Hu, Y. R. Shou, B. Qiao, C. E. Chen, X. T. He, S. S. Bulanov, T. Z. Esirkepov, S. V. Bulanov, and X. Q. Yan, High-efficiency  $\gamma$ -ray flash generation via multiple-laser scattering in ponderomotive potential well, *Phys. Rev. E* **95**, 013210 (2017).
- [44] T. Grismayer, M. Vranic, J. L. Martins, R. A. Fonseca, and L. O. Silva, Seeded QED cascades in counterpropagating laser pulses, *Phys. Rev. E* **95**, 023210 (2017).
- [45] T. Grismayer, M. Vranic, J. L. Martins, R. A. Fonseca, and L. O. Silva, Laser absorption via quantum electrodynamics cascades in counter propagating laser pulses, *Phys. Plasmas* **23**, 056706 (2016).
- [46] M. Jirka, O. Klimo, S. V. Bulanov, T. Z. Esirkepov, E. Gelfer, S. S. Bulanov, S. Weber, and G. Korn, Electron dynamics and  $\gamma$  and  $e^-e^+$  production by colliding laser pulses, *Phys. Rev. E* **93**, 023207 (2016).
- [47] Q. Z. Lv, E. Raicher, C. H. Keitel, and K. Z. Hatsagortsyan, High-brilliance ultranarrow-band x rays via electron radiation in colliding laser pulses, *Phys. Rev. Lett.* **128**, 024801 (2022).

- [48] E. Brezin and C. Itzykson, Pair production in vacuum by an alternating field, *Phys. Rev. D* **2**, 1191 (1970).
- [49] E. Raicher and K. Z. Hatsagortsyan, Nonlinear QED in an ultrastrong rotating electric field: Signatures of the momentum-dependent effective mass, *Phys. Rev. Res.* **2**, 013240 (2020).
- [50] S. Villalba-Chávez and C. Müller, Signatures of the Schwinger mechanism assisted by a fast-oscillating electric field, *Phys. Rev. D* **100**, 116018 (2019).
- [51] R. Schützhold, H. Gies, and G. Dunne, Dynamically assisted Schwinger mechanism, *Phys. Rev. Lett.* **101**, 130404 (2008).
- [52] J. G. Kirk, Radiative trapping in intense laser beams, *Plasma Phys. Control. Fusion* **58**, 085005 (2016).
- [53] P. L. Kapitza and P. A. M. Dirac, The reflection of electrons from standing light waves, *Math. Proc. Cambridge Philos. Soc.* **29**, 297 (1933).
- [54] H. Batelaan, Colloquium: Illuminating the Kapitza-Dirac effect with electron matter optics, *Rev. Mod. Phys.* **79**, 929 (2007).
- [55] S. Ahrens, H. Bauke, C. H. Keitel, and C. Müller, Spin dynamics in the Kapitza-Dirac effect, *Phys. Rev. Lett.* **109**, 043601 (2012).
- [56] M. M. Dellweg and C. Müller, Spin-polarizing interferometric beam splitter for free electrons, *Phys. Rev. Lett.* **118**, 070403 (2017).
- [57] A. Friedman, A. Gover, G. Kurizki, S. Ruschin, and A. Yariv, Spontaneous and stimulated emission from quasifree electrons, *Rev. Mod. Phys.* **60**, 471 (1988).
- [58] R. Pantell, G. Soncini, and H. Puthoff, Stimulated photon-electron scattering, *IEEE J. Quantum Electron.* **4**, 905 (1968).
- [59] M. V. Fedorov, Free-electron lasers and multiphoton free-free transitions, *Prog. Quantum Electron.* **7**, 73 (1981).
- [60] H. K. Avetissian, *Relativistic Nonlinear Electrodynamics* (Springer, New York, 2016).
- [61] E. L. Saldin, E. A. Schneidmiller, and M. V. Yurkov, The physics of free electron lasers. An introduction, *Phys. Rep.* **260**, 187 (1995).
- [62] B. King and H. Hu, Classical and quantum dynamics of a charged scalar particle in a background of two counterpropagating plane waves, *Phys. Rev. D* **94**, 125010 (2016).
- [63] H. Hu and J. Huang, Analytical solution for the Klein-Gordon equation and action function of the solution for the Dirac equation in counterpropagating laser waves, *Phys. Rev. A* **92**, 062105 (2015).
- [64] Q. Z. Lv, E. Raicher, C. H. Keitel, and K. Z. Hatsagortsyan, Ultrarelativistic electrons in counterpropagating laser beams, *New J. Phys.* **23**, 065005 (2021).
- [65] V. I. Ritus, Quantum effects of the interaction of elementary particles with an intense electromagnetic field, *J. Sov. Laser Res.* **6**, 497 (1985).
- [66] A. Otto, D. Seipt, D. Blaschke, S. A. Smolyansky, and B. Kämpfer, Dynamical Schwinger process in a bifrequent electric field of finite duration: Survey on amplification, *Phys. Rev. D* **91**, 105018 (2015).
- [67] C. Schneider and R. Schützhold, Dynamically assisted Sauter-Schwinger effect in inhomogeneous electric fields, *J. High Energy Phys.* **02** (2016) 164.
- [68] G. Torgrimsson, C. Schneider, J. Oertel, and R. Schützhold, Dynamically assisted Sauter-Schwinger effect — non-perturbative versus perturbative aspects, *J. High Energy Phys.* **06** (2017) 043.
- [69] G. Torgrimsson, C. Schneider, and R. Schützhold, Sauter-Schwinger pair creation dynamically assisted by a plane wave, *Phys. Rev. D* **97**, 096004 (2018).
- [70] M. F. Linder, C. Schneider, J. Sicking, N. Szpak, and R. Schützhold, Pulse shape dependence in the dynamically assisted Sauter-Schwinger effect, *Phys. Rev. D* **92**, 085009 (2015).
- [71] I. A. Aleksandrov, G. Plunien, and V. M. Shabaev, Dynamically assisted Schwinger effect beyond the spatially-uniform-field approximation, *Phys. Rev. D* **97**, 116001 (2018).
- [72] A. Di Piazza, E. Lötstedt, A. I. Milstein, and C. H. Keitel, Barrier control in tunneling  $e^+ - e^-$  photoproduction, *Phys. Rev. Lett.* **103**, 170403 (2009).